# nature communications



**Article** 

https://doi.org/10.1038/s41467-024-53853-7

# Time-efficient atmospheric water harvesting using Fluorophenyl oligomer incorporated MOFs

Received: 2 November 2023

Accepted: 23 October 2024

Published online: 12 November 2024

Check for updates

Min Seok Kang  $\mathbb{O}^{1,5}$ , Incheol Heo  $\mathbb{O}^{1,5}$ , Sun Ho Park  $\mathbb{O}^{2,5}$ , Jinhee Bae  $\mathbb{O}^2$ , Sangyeop Kim  $\mathbb{O}^1$ , Gyuchan Kim  $\mathbb{O}^1$ , Byung-Hyun Kim  $\mathbb{O}^{1,3}$ , Nak Cheon Jeong  $\mathbb{O}^{2,4} \boxtimes \mathbb{O}$  & Won Cheol Yoo  $\mathbb{O}^{1,3} \boxtimes \mathbb{O}$ 

Adsorption-based atmospheric water harvesting (AWH) has the potential to address water scarcity in arid regions. However, developing adsorbents that effectively capture water at a low relative humidity (RH < 30%) and release it with minimal energy consumption remains a challenge. Herein, we report a fluorophenyl oligomer (FO)-incorporated metal-organic framework (MOF), HKUST-1 (FO@HK), which exhibits fast adsorption kinetics at low RH levels and facile desorption by sunlight. The incorporated fluorophenyl undergoes vapor-phase polymerization at the metal center to generate fluorophenyl oligomers that enhance the hydrolytic stability of FO@HK while preserving its characteristic water sorption behavior. The FO@HK exhibited vapor sorption rates of 8.04 and 11.76 L kg $^{-1}_{MOF}$  h $^{-1}$  at 20 and 30% RH, respectively, which are better than the state-of-the-art AWH sorbents. Outdoor tests using a solar-driven large-scale AWH device demonstrate that the sorbent can harvest 264.8 mL of water at a rate of 2.62 L kg $^{-1}_{MOF}$  per day. This study provides a ubiquitous strategy for transforming water-sensitive MOFs into AWH sorbents.

As two-thirds of the world's population is experiencing water scarcity, which is mainly attributed to population growth, climate change, and complicated factors, the demand for fresh water has become increasingly important<sup>1,2</sup>. Among various technologies, atmospheric water harvesting (AWH) has received great attention because it is not restricted by regional conditions<sup>3–5</sup>. In arid regions that experience severe water shortages, a technique that can be operated under low relative humidity (RH < 30%) and with minimum energy consumption has been of great interest<sup>3,6–8</sup>. In this regard, well-known atmospheric water-capturing methods, such as fog capture<sup>9,10</sup>, which is operable under high RH, and dew condensation<sup>11,12</sup>, which usually requires a large amount of energy, are not promising candidates. For time-efficient AWH at a low RH, sorbents should exhibit the following requirements: water stability for multiple water adsorption-desorption

cycles, high water uptake with fast sorption kinetics at low RH conditions (<30%), and low energy consumption for water desorption<sup>5,13</sup>.

For instance, zeolites have demonstrated adequate adsorption abilities for operation over a wide range of RHs, and silica gels have shown reduced water adsorption at low RHs. In addition, these adsorbents usually require high energy for water desorption and exhibit relatively low water uptake capacities<sup>14,15</sup>. Polymer-based sorbents exhibit excellent water uptake capacities with relatively low energy consumption for water desorption; however, few polymeric sorbents with fast sorption kinetics under low RH conditions have been reported<sup>8,16-21</sup>. It has also been reported that balancing the hydrophilic and hydrophobic properties of covalent organic frameworks (COFs) is important for improving the sorption kinetics in AWH systems<sup>22</sup>. Recently, metal-organic frameworks (MOFs), which are

crystalline coordination compounds composed of metal nodes and organic linkers with microporosity and chemical diversity, have exhibited promising results and are suitable for AWH in arid areas<sup>23–25</sup>.

For example, Zr-containing MOF-801 exhibited efficient AWH abilities at humidity levels down to 20% RH and was powered by natural sunlight. Solar-driven thermal heating enabled water desorption from the MOF, resulting in 2.8 L kg<sup>-1</sup> of water harvested per day at 20% RH<sup>3</sup>. This result is noteworthy because the characteristic water sorption isotherm of MOF-801 exhibits a sharp increase at very low relative pressures. Thus, this MOF is suitable for high water uptake at a low RH and fast desorption by low-grade energy sources, such as sunlight. In addition, Al-containing MOF-303 exhibited a faster vapor sorption rate of 4.8 L kg<sup>-1</sup> h<sup>-1</sup> at 30% RH than MOF-801, proving the applicability of MOFs for AWH in arid regions<sup>26</sup>. Based on previous results, hydrolytic stability and characteristic water sorption behavior are noted as important features when applying MOFs for energy-efficient AWH applications<sup>23,24</sup>.

Herein, we report the most time-efficient solar-driven AWH of fluorophenyl oligomer-incorporated HKUST-1 (hereafter denoted as FO@HK, where HK is a completely desolvated MOF, HKUST-1). Vaporphase polymerization (VPP) of a few phenolic precursors, including fluorine-free, mono-fluorine, and tri-fluorine phenols (denoted as  $F_0$ ,  $F_1$ , and  $F_3$ , respectively), was performed at the metal center, resulting in the formation of the corresponding polymers in the pores of HKUST-1 (denoted as  $F_0$ @HK,  $F_1$ @HK, and  $F_3$ @HK, respectively). We found that the incorporation of FO substantially enhanced the hydrolytic stability of HKUST-1. This improvement can be attributed to two factors: (i) the protection of open Cu(II) sites from water coordination through dynamic coordination of the hydroxyl oxygen in the fluorophenol moiety, and (ii) the increase in hydrophobicity achieved by using fluorinated oligomers while retaining the characteristic water sorption behavior of HKUST-1.

Among the various FO@HK samples,  $F_3$ @HK with a porosity blockage of 30% (denoted as  $F_3$ @HK\_30), compared to pristine HKUST-1 (hereafter pristine-HK), demonstrated excellent vapor sorption rates of 3.84, 8.04, and 11.76 L kg $^{-1}$ MOF h $^{-1}$  at 10, 20, and 30% RH, respectively. This represents the best value known to date and excellent water sorption kinetics. In addition, a solar-driven AWH device based on  $F_3$ @HK\_30 with carbon paper exhibited an adsorption capacity of 0.23 g g $^{-1}$ MOF at 25% RH within 10 min and desorption under 1 sun condition within 20 min in the indoor experiment. This device could harvest 10.08 L kg $^{-1}$ MOF of water daily without additional energy input. Therefore, this strategy can be ubiquitously applied to watersensitive MOFs with characteristic water sorption behavior, making them time-efficient sorbents for AWH to sustainably provide fresh water in arid regions.

# Results

#### Fluorophenyl oligomer-incorporated MOFs prepared by VPP

HKUST-1 (Cu<sub>3</sub>BTC<sub>2</sub>, BTC = 1, 3, 5 benzene tricarboxylate), a well-known MOF, has a characteristic water sorption behavior suitable for capturing water at low RHs (Fig. 1a). However, its inherent instability under hydrolytic conditions limits its water sorption applications<sup>27,28</sup>. Thus, for AWH applications under dry conditions, the hydrolytic stability of HKUST-1 should be significantly improved while preserving its characteristic water sorption behavior. Therefore, a VPP strategy was used to prepare an FO@HK composite to improve the hydrolytic stability of pristine HK, which was employed as a sorbent for AWH under arid conditions (Fig. 1b)29-31. VPP preferentially occurs at open Cu(II) sites, effectively serving as a Lewis acid catalyst for polymerization and resulting in enhanced hydrolytic stability. We attribute this improvement to the protection of the open Cu(II) sites against water coordination via the dynamic coordination of the hydroxyl oxygen within the fluorophenol moiety, thereby retaining its inherent water sorption characteristics (Fig. 1c). First, different amounts of the fluorine-free phenol-formaldehyde precursor (F<sub>0</sub>) were used for the VPP reaction in HK at 90 °C for 12 h. The nitrogen sorption isotherms (Supplementary Fig. 1) showed a gradual decrease in the micropore volume with higher  $F_0$  amounts for the  $F_0$ @HK samples, while the type I characteristic isotherms for the samples were retained. With increasing precursor amounts, the micropore volumes of the F<sub>0</sub>@HK samples decreased to 5, 15, and 30%, respectively (hereafter denoted as F<sub>0</sub>@HK 5, F<sub>0</sub>@HK 15, and F<sub>0</sub>@HK 30; Supplementary Table 1). The surface state, morphological features, and crystallinity of the F<sub>0</sub>@HK samples were monitored using scanning electron microscopy (SEM) and powder X-ray diffraction (PXRD), and it was found that the features were the same as those of pristine HK (Supplementary Figs. 1, 2). By combining the above results, we concluded that VPP could preserve the characteristic isotherm type, crystallinity, and morphology of pristine-HK, except for a controllable reduction in microporosity. In addition, the pores of pristine-HK were eventually blocked by prolonged polymerization with a greater amount of the precursor, denoted as F<sub>0</sub>@HK 100, which also presented a smooth surface morphology and preserved the crystallinity of pristine-HK (Supplementary Fig. 1 and Supplementary Table 1).

Because fluorinated MOFs have shown improved hydrophobicity, especially toward water vapor $^{32-34}$ , we employed fluorine-substituted phenols ( $F_1$  and  $F_3$ ) as precursors in further VPP. As expected, a gradual reduction in microporosity with higher amounts of  $F_1$  and  $F_3$  precursors equivalent to those used for the  $F_0$ @HK samples was clearly identified in the  $F_1$ @HK\_5,  $F_1$ @HK\_15, and  $F_1$ @HK\_30 samples, and the  $F_3$ @HK\_5,  $F_3$ @HK\_15, and  $F_3$ @HK\_30 samples (Fig. 1d, Supplementary Fig. 3, and Supplementary Table 1), while they preserved the type-l isotherms well. Furthermore, the SEM and PXRD results indicated that the surface state, morphological features, and crystallinity were also well maintained for the  $F_1$ @HK and  $F_3$ @HK samples after VPP (Fig. 1e, f and Supplementary Figs. 3, 4).

VPP was successfully achieved via an acid-catalyzed reaction involving the addition of a phenol to formaldehyde to form hydroxymethyl derivatives, followed by condensation to form methylene and methylene ether-bridged derivatives<sup>35</sup>. To elucidate the chemical structure of the synthesized polymeric species within the pores of pristine-HK, we performed digestion <sup>1</sup>H NMR measurements on the pristine-HK, F<sub>3</sub>@HK 30, and F<sub>3</sub>@HK 100 samples (Fig. 1g and Supplementary Figs. 5, 6). In the F<sub>3</sub>@HK\_100 sample, the peaks at 2.78 and 2.61 ppm were assigned to the protons of the methylene ether bridge and methylene bridge between fluorophenols, respectively. These peaks indicate the presence of polymeric moieties in the F<sub>3</sub>@HK\_100 sample, as they were not observed in the pristine-HK spectrum. Conversely, in the F<sub>3</sub>@HK\_30 sample, a decrease in the intensity of the peaks associated with methylene ether and methylene bridges was observed. Instead, a peak at 1.89 ppm was observed, corresponding to the methylene bridge proton of the hydroxymethyl group. This suggested that a complete condensation reaction was not achieved for the F<sub>3</sub>@HK 30 sample. The fluorophenol moieties were quantified using <sup>1</sup>H NMR spectroscopy and calibrated using a BTC linker as internal standard. The results revealed that the molar ratios of Cu:fluorophenol in F<sub>3</sub>@HK\_100 and F<sub>3</sub>@HK\_30 were approximately 1:2.78 and 1:0.68, respectively (Supplementary Tables 2-6). These ratios closely corresponded to the proportions of reactants used during the synthesis.

The atomic percentages of fluorine in the  $F_3@HK\_15$  and  $F_3@HK\_30$  samples were 3.8 and 6.3%, respectively, as determined using energy-dispersive X-ray spectroscopy (EDX) during SEM measurements (Supplementary Fig. 7 and Table 7). The EDX results indicated that the molar ratios of Cu:fluorophenol in  $F_3@HK\_15$  and  $F_3@HK\_30$  were approximately 1:0.29 and 1:0.62, respectively, which were similar to the proportions used for synthesis. Thermogravimetric analysis (TGA) confirmed the Cu: fluorophenol ratio of 0.70 for  $F_3@HK\_30$  (Supplementary Fig. 8 and Supplementary Note 2).

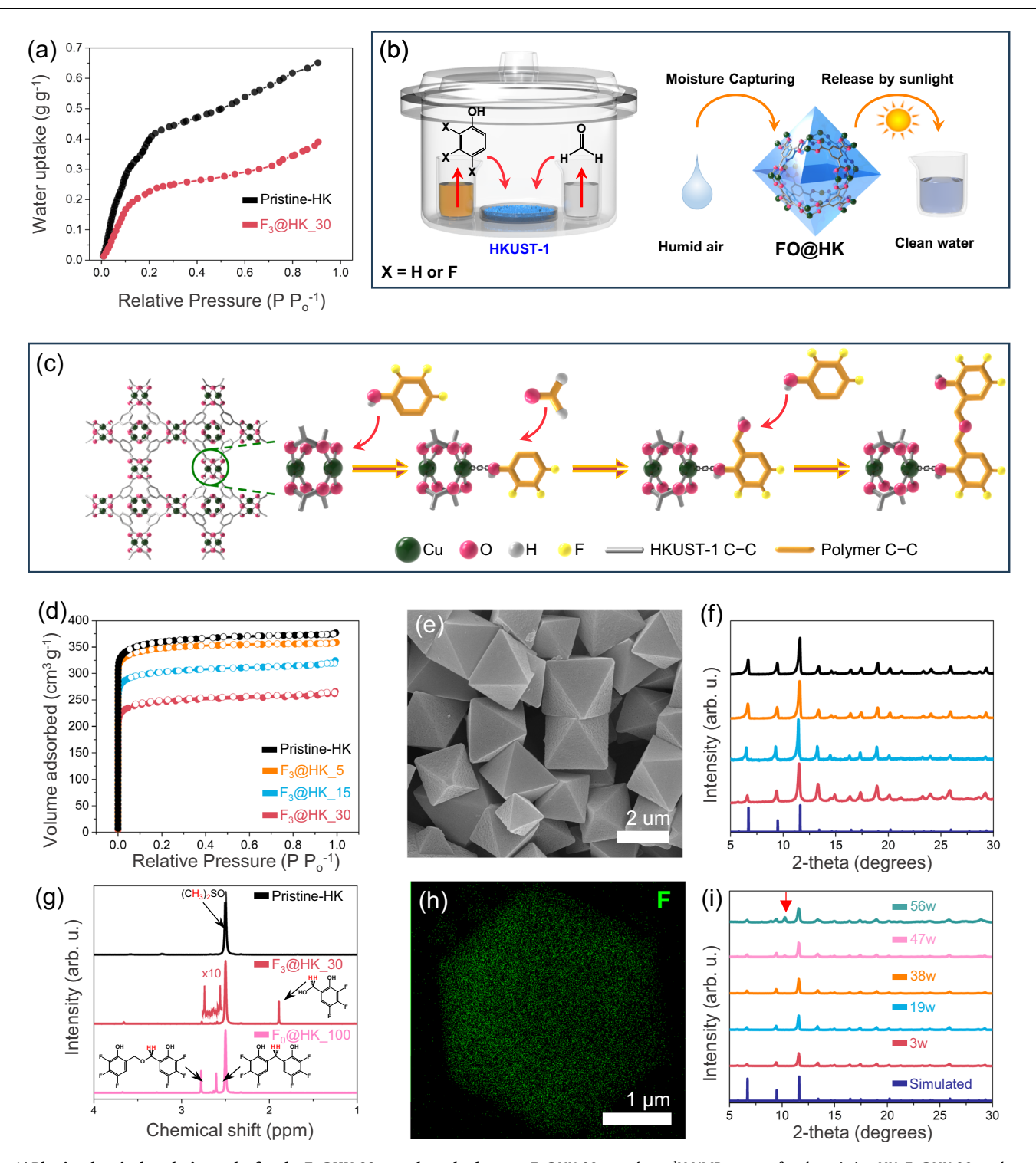


**Fig. 1** | **Physicochemical analysis results for the F**<sub>3</sub>@**HK**\_3**0 sample and schematic illustrations of VPP and AWH.** a Water sorption isotherms for pristine-HK and F<sub>3</sub>@**HK**\_30 at 298 K. **b**, **c** (**b**) Schematic illustrations of synthesizing FO@**HK** for AWH, and (**c**) VPP processes preferentially occurring at open Cu sites that act as Lewis acid catalysts for polymerization within the pores of pristine-HK. **d** Nitrogen sorption isotherms for F<sub>3</sub>@**HK**\_5, F<sub>3</sub>@**HK**\_15, and F<sub>3</sub>@**HK**\_30 indicate a gradual decrease in micropore volumes with increasing precursor amounts. **e** SEM image of F<sub>3</sub>@**HK**\_30. **f** PXRD results of the pristine-HK and F<sub>3</sub>@**HK**\_5, F<sub>3</sub>@**HK**\_15, and

 $F_3@HK_30$  samples. g  $^1H$  NMR spectra for the pristine-HK,  $F_3@HK_30$ , and  $F_0@HK_100$  samples.  $^1H$  NMR was taken after the crystals were completely digested in DMSO-d<sub>6</sub> with  $D_2SO_4$ . h HAADF elementary F mapping image for the  $F_3@HK_30$  sample. i PXRD results for the  $F_3@HK_30$  sample under harsh condition (88 °C with 88% RH). The red arrow displayed in the PXRD results indicates a crystalline phase transition to the non-porous phase after exposure to hot humid air. Source data are provided as a Source Data file.

In addition, high-angle annular dark field (HAADF) element mapping analysis, carried out in scanning transmission electron microscopy (STEM) mode, demonstrated that Cu, C, and O were spatially well distributed in the F<sub>3</sub>@HK\_30 sample (Supplementary Fig. 9). More

importantly, the F-mapping image showed that the fluorophenyl oligomer was evenly distributed within the pores of the pristine-HK crystal rather than residing on its surface (Fig. 1h and Supplementary Fig. 10).

#### Enhanced hydrolytic stability of FO@MOFs

As it is interesting to determine the extent to which the VPP process improves the hydrolytic stability of FO@HK, the pristine-HK and F<sub>0</sub>@HK 15, F<sub>1</sub>@HK 15, F<sub>3</sub>@HK 15, and F<sub>3</sub>@HK 30 samples were tested under harsh condition (88 °C with 88% RH). According to the PXRD results shown in Fig. 1i and Supplementary Fig. 11, the crystalline phase of pristine-HK was significantly changed to a non-porous phase after exposure to humid air for 18 h at 88 °C with 88% RH. In contrast, the PXRD results showed that the hydrolytic stability of the polymer@HK samples was substantially improved compared to that of pristine-HK. The  $F_0$ @HK 15,  $F_1$ @HK 15, and  $F_3$ @HK 15 samples retained their crystallinities much longer and began to change to the nonporous phase slightly after exposure for 3, 7, and 9 weeks, respectively. Considering that the polymer@HK 15 samples retained 85% porosity, VPP can be considered a highly effective strategy to improve hydrolytic stability. In addition, samples with more fluorine substituents exhibited higher hydrolytic stability in the order of  $F_0$ @HK 15 <  $F_1$ @HK 15 <  $F_3$ @HK 15, clearly demonstrating the positive effects of fluorination. Surprisingly, the hydrolytic stability of the F<sub>3</sub>@HK 30 sample was significantly enhanced and its crystallinity remained intact even when the fluorinated MOF was exposed at 88 °C with 88% RH for 56 weeks. In addition, nitrogen sorption isotherms were attempted for the F<sub>3</sub>@HK\_30 sample after 38 and 56 weeks, and their microporosities were 0.22 and 0.11 cm<sup>3</sup> g<sup>-1</sup>, respectively (Supplementary Fig. 12 and Table 1) even under harsh condition (88 °C and RH 88%). This suggests that more than 50% of the porosity of F<sub>3</sub>@HK\_30 can be used for almost 9 months, even under such harsh condition. Based on this result, we hypothesized that the open Cu (II) sites could be protectively coordinated with fluorophenol moieties, where water molecules can coordinate and consequently damage the crystallinity<sup>36-38</sup>. Therefore, the enhanced hydrolytic stability of the FO@HK samples was attributed to the coordinative protection of the fluorophenol moieties by a combination of fluorination effects. This approach was applied to MOF-74 (Mg), which has open metal sites. F<sub>3</sub>@MOF-74(Mg) 30 (30% of the micropores of pristine MOF-74(Mg) were decreased by VPP) was successfully prepared and exhibited improved hydrolytic stability compared to the pristine MOF-74(Mg) (Supplementary Fig. 13 and Supplementary Discussion 1).

# Dynamic coordination of oxygen moieties to Cu(II) sites

To test this hypothesis, ex situ and in situ Raman spectroscopy measurements were performed, predicting that the vibrational band of the Cu-Cu nodes in HKUST-1 is sensitively altered upon coordination bonding of axially associated atoms or molecules. Additionally, the measurements were used to determine whether the hydroxyl oxygen in the FO is associated based on the vibrational frequency (Fig. 2). We first conducted ex-situ Raman measurements on the activated F<sub>3</sub>@HK\_30 and F<sub>3</sub>@HK\_15 (Act-F<sub>3</sub>@HK\_30 and Act-F<sub>3</sub>@HK\_15) samples. For comparison, we also conducted measurements using activated pristine-HK (Act-HK). Furthermore, we performed measurements with water-exposed Act-F<sub>3</sub>@HK\_30, Act-F<sub>3</sub>@HK\_15, and Act-HK samples (H<sub>2</sub>O-F<sub>3</sub>@HK 30, H<sub>2</sub>O-F<sub>3</sub>@HK 15, and H<sub>2</sub>O-HK, respectively) to monitor spectral changes. As a result, while the Cu-Cu stretching band at approximately 230 cm<sup>-1</sup>, which originates from the open Cu(II) state (a non-coordinating state at the axial position)<sup>36–38</sup>, appeared in all Act-F<sub>3</sub>@HK\_30, Act-F<sub>3</sub>@HK\_15, and Act-HK samples, the stretching vibration at 169 cm<sup>-1</sup> appeared only in the Act-F<sub>3</sub>@HK\_30 and Act-F<sub>3</sub>@HK\_15 samples (Supplementary Fig. 14). When the Act-F<sub>3</sub>@HK 15 sample was exposed to moist air (H<sub>2</sub>O-F<sub>3</sub>@HK 15), the vibrational bands at 229 cm<sup>-1</sup> disappeared, and the band at 169 cm<sup>-1</sup> shifted slightly to 177 cm<sup>-1 38</sup>. This pattern is similar to that observed for H<sub>2</sub>O-HK. Thus, the 169 cm<sup>-1</sup> vibrational band in Act-F<sub>3</sub>@HK\_15 was attributed to coordination bonding of the hydroxyl oxygen in the fluorophenyl moieties, and the band shifted to 173 cm<sup>-1</sup> under moist conditions with the association of water molecules at the Cu(II) sites after the dissociation of the hydroxyl oxygens. In contrast,  $H_2O\text{-}F_3@HK\_30$  exhibited the same Raman spectrum as Act-F<sub>3</sub>@HK\_30, clearly confirming that the Cu(II) sites were stably coordinated to the hydroxyl oxygen in the fluorophenyl moieties, even under humid conditions.

To corroborate the slight band shift from  $169 \text{ cm}^{-1}$  to  $173 \text{ cm}^{-1}$ , we performed in situ Raman spectroscopy measurements on the Act-F<sub>3</sub>@HK\_30 and Act-F<sub>3</sub>@HK\_15 samples, successively exposing them to moist air (Fig. 2a, b). As expected, while the vibrational band at  $229 \text{ cm}^{-1}$  for Act-F<sub>3</sub>@HK\_15 disappeared, that at  $169 \text{ cm}^{-1}$  shifted to  $177 \text{ cm}^{-1}$  when the sample was exposed to moist air. Thus, we attributed the band shift to the dynamic coordination exchange of the hydroxyl oxygens of fluorophenols with water molecules at the axial Cu(II) sites (Fig. 2c). In contrast, for the Act-F<sub>3</sub>@HK\_30 sample, the peaks at 169 and  $229 \text{ cm}^{-1}$  remained intact for 120 min under in situ Raman spectroscopy with continuous exposure to humid air (Fig. 2b). This result implies that the coordination bond between the Cu(II) sites and hydroxyl oxygens of Act-F<sub>3</sub>@HK\_30 (prepared with twice the amount of fluorophenol precursor compared to Act-F<sub>3</sub>@HK\_15) was mostly intact even after exposure to water (Fig. 2c).

To investigate our hypothesis concerning the coordinative protection afforded by the fluorophenyl oligomer at open Cu(II) sites, density functional theory (DFT) calculations were conducted to analyze the interactions between the fluorophenyl oligomer and water at these sites. The adsorption energy of a water molecule at the Cu(II) site was calculated to be -0.61 eV, with a bond length of 2.271 Å (Fig. 2d and Supplementary Fig. 15a), consistent with results reported previously<sup>39,40</sup>. In contrast, the adsorption energy of the phenolic oxygen of the fluorophenyl oligomer was -1.73 eV, indicating a significantly stronger adsorption compared to that of water. The stronger adsorption of the fluorophenyl oligomer was attributed to the adsorption geometry within the pristine-HK pore structure (Fig. 2d and Supplementary Fig. 15b). Specifically, the phenolic oxygen of the fluorophenyl oligomer bonds with the open Cu(II) site, exhibiting a bond length of 2.397 Å, and additional hydrogen bonding occurs between the hydroxyl hydrogen and carboxylate at the adjacent Cu(II) site, with a bond length of 1.938 Å. Notably, the observed adsorption geometry represents the maximum adsorption strength of the fluorophenyl oligomer, assuming that no other molecules are adsorbed on the open Cu(II) sites. Under actual conditions, where the Cu sites may interact with or be blocked by other molecules, the difference in the adsorption energy between the fluorophenyl oligomer and water could be less pronounced. Nevertheless, DFT calculations successfully demonstrated that fluorophenyl oligomers can effectively protect open Cu(II) sites from water, exhibiting comparable or even stronger interactions.

By combining the aforementioned results, we hypothesize that VPP occurs at open Cu(II) sites in pristine-HK (Fig. 2e). It should be noted that HKUST-1 is composed of two types of large cages (type-I and -II) and a small cage (type-III). All open Cu(II) sites face the internal pores of the type-I large cage, whereas the type-II large cage and type-III small cage do not have open Cu(II) sites facing the interior of the pores (Supplementary Fig. 16 and Supplementary Discussion 2). Thus, it is reasonable to infer that VPP preferentially occurs in the type-I large cages, whereas the pores of the type-II large cages and type-III small cages remain almost intact until the type-I large pores are filled (Fig. 2e). Simulations based on the size of the type-I large cage and hydroxymethyl fluorophenol showed that the pores of the type-I cage were almost entirely filled with the quantity of hydroxymethyl fluorophenol used in F<sub>3</sub>@HK 30 (Supplementary Fig. 17 and Supplementary Discussion 3). Therefore, the super-enhanced hydrolytic stability of F<sub>3</sub>@HK\_30 can be attributed to the effective dynamic coordination of the phenolic oxygen of the fluorophenyl oligomer to the open Cu(II) site and hydrogen bonding with the carboxylate located at the adjacent open Cu(II) site. In addition to the hydrophobic property of

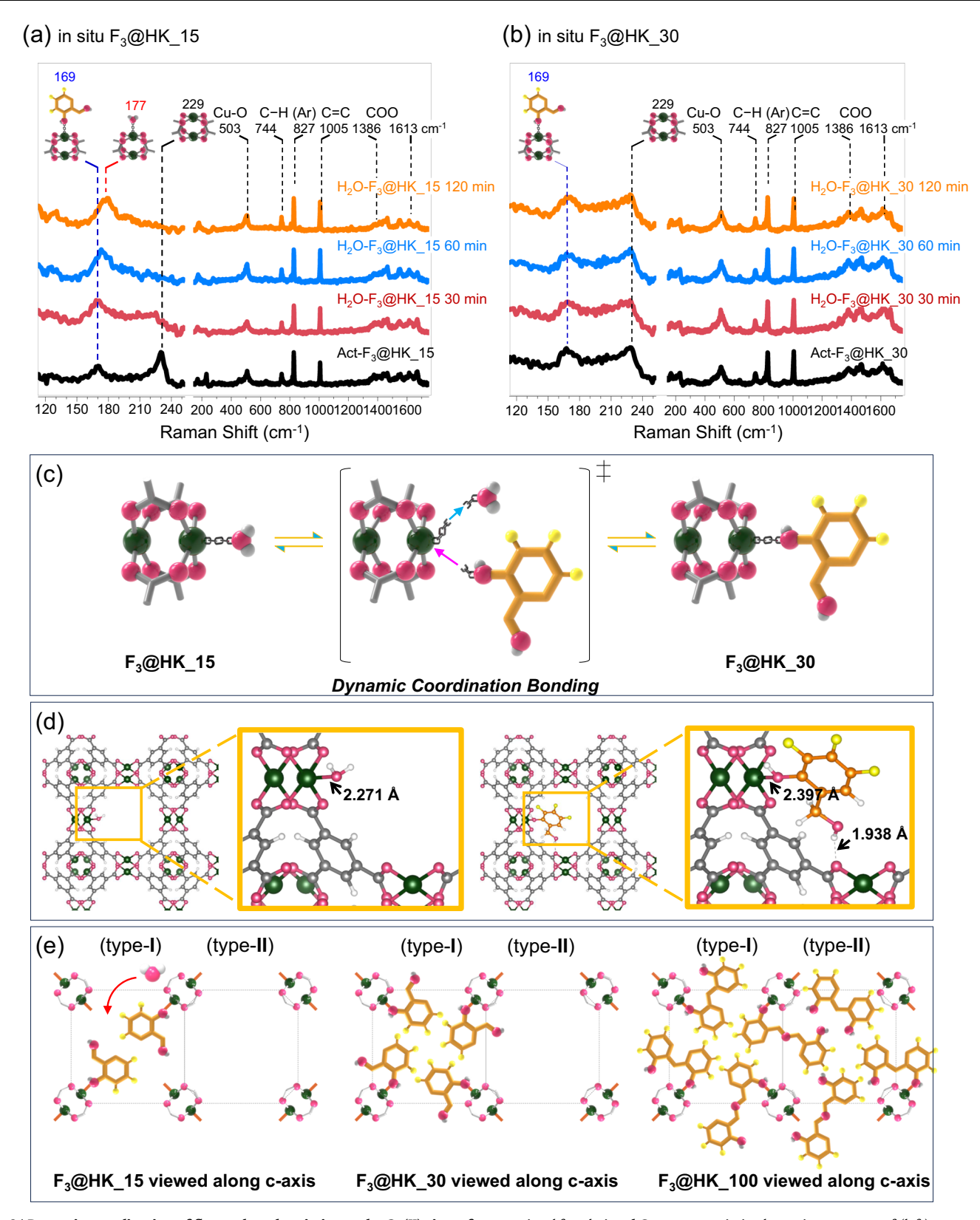
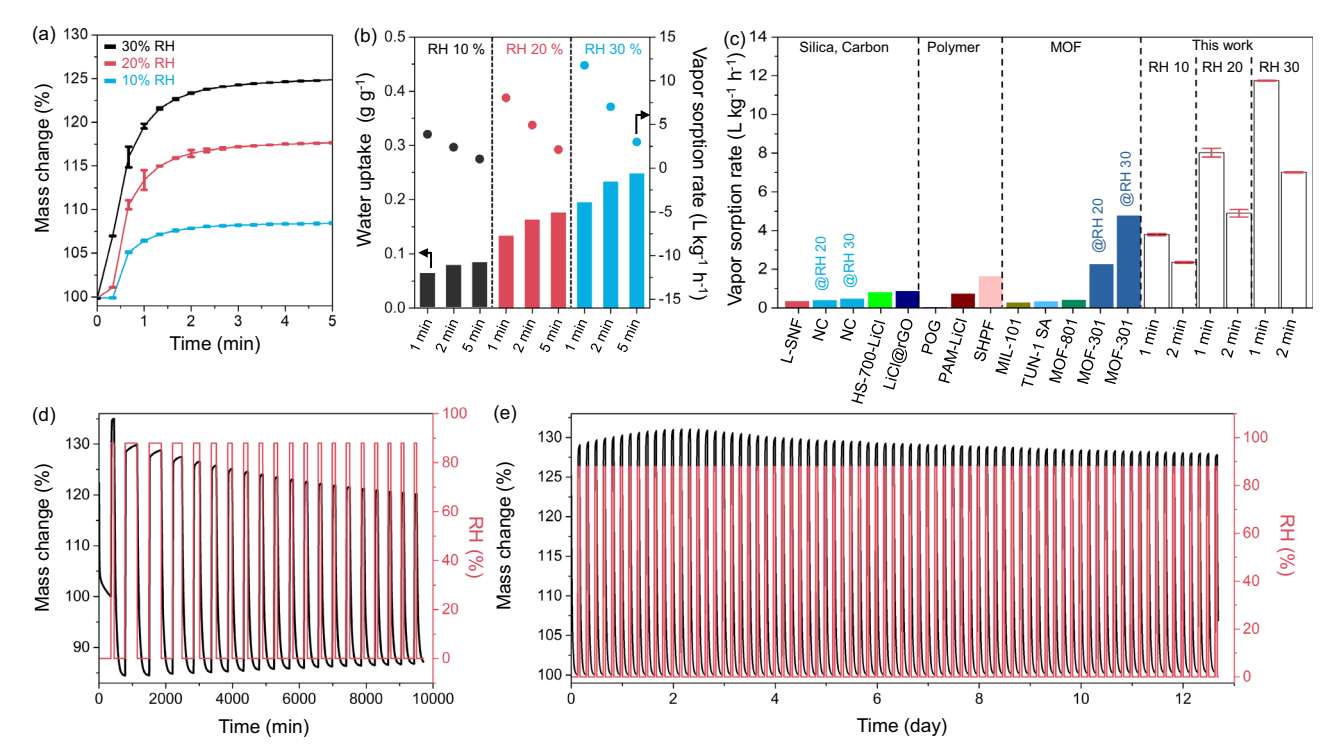


Fig. 2 | Dynamic coordination of fluorophenol moieties to the Cu(II) sites of pristine-HK and a proposed hypothesis demonstrating VPP at the open Cu(II) sites. a, b In situ Raman spectra obtained every 30, 60, and 120 min for the (a) Act-F<sub>3</sub>@HK\_15, and (b) Act-F<sub>3</sub>@HK\_30 samples under exposure to moist air, respectively. Characteristic peaks in both Raman spectra were assigned to the corresponding vibration modes. c Schematic illustration of "dynamic coordination exchange" of the hydroxyl oxygen of fluorophenol and water molecules at the axial Cu(II) sites. Hydrogen atoms bonded to carbon atoms in the benzene moieties are

omitted for clarity. **d** Geometry-optimized atomic structures of (left) water-adsorbed and (right) fluorophenol-adsorbed HKUST-1. The gray, green, pink, and white spheres represent C, Cu, O, and H atoms, respectively. For clarity, the C atoms in fluorophenol are colored orange. **e** Schematic illustration of a proposed hypothesis exhibiting a gradual polymerization starting from the type-I large cage where all the open Cu(II) sites are located, and then subsequent polymerization eventually occupying the type-II large cage. Polymerization through the type-III small cage was omitted for clarity. Source data are provided as a Source Data file.



**Fig. 3** | **DVS results of the pristine-HK and F**<sub>3</sub>@**HK**\_3**0 samples under different RH conditions.** a DVS profiles of F<sub>3</sub>@**HK**\_30 with different RH conditions (10, 20, and 30% RH). The error bars represent the standard deviation of the triplicate mass change measurements. **b** Water uptakes (left y-axis) and vapor sorption rates (right y-axis) of the F<sub>3</sub>@**HK**\_30 sample at different uptake times under different RH conditions. **c** Comparison of the vapor sorption rates of various sorbents including silica, carbon, polymer, and MOF with the F<sub>3</sub>@**HK**\_30 sample at low RH levels. If the

reference sorbents have several vapor sorption rates below 30% RH, then those values are also included. The vapor sorption rates of  $F_3$ @HK\_30 obtained from different uptake times under different RH conditions are listed for comparison. The error bars represent the standard deviation of the triplicate vapor sorption rate measurements. **d**, **e** Multi-cycle DVS results for (**d**) pristine-HK and (**e**)  $F_3$ @HK\_30 with vapor adsorption under 88% RH at 25 °C and desorption by the pressure swing of nitrogen gas at 25 °C. Source data are provided as a Source Data file.

 $F_3$ @HK\_30 due to the fluorination effect, the type-I large cages with all open Cu(II) sites facing inward were substantially protected from water vapor, whereas the type-II large cages and type-III small cages still have sufficient space to allow guest molecules to be freely accessible. Eventually, the type-II large cages and type-III small cages are occupied by the polymer via a prolonged VPP process, forming  $F_3$ @HK\_100 (Fig. 2e).

# Dynamic vapor sorption measurements

Owing to its hydrolytic stability compared to other samples, water sorption experiments were performed on the F<sub>3</sub>@HK\_30 sample. Dynamic vapor sorption (DVS) was performed for the F<sub>3</sub>@HK\_30 sample three times under various RHs, including 10, 20, and 30% at 25 °C. The DVS profiles of F<sub>3</sub>@HK\_30 at different RHs (Fig. 3a) showed that all the samples exhibited similar and very fast vapor sorption dynamics. The experiments were conducted in triplicate, and error bars were calculated for each point using the standard deviation. For the specific measurement, the vapor sorption capacities at different RHs (10, 20, and 30%) were 0.084, 0.177, and 0.249 g g<sup>-1</sup><sub>MOF</sub>, respectively, which were achieved within 5 min. Sorption capacities greater than 70% (76.2, 75.7, and 78.7% at 10, 20, and 30% RH, respectively) were achieved within 1 min for all RHs (Fig. 3b). The corresponding vapor sorption rates for 10, 20, and 30% RH at 1 min were 3.84, 8.04, and 11.76 L  $kg^{-1}_{MOF}$   $h^{-1}$ , respectively, and those at 2 min were 2.37, 4.92, and  $7.02 \, \text{L kg}^{-1}_{\text{MOF}} \, \text{h}^{-1}$ , respectively (Fig. 3b). The other two results are shown in Fig. 3a, c and in Supplementary Table 8. To the best of our knowledge, under low RH conditions (<30%), these vapor sorption rates are among the best values reported to date (Fig. 3c and Supplementary Table 8<sup>6,8,19,20,26,41-45</sup>). Error bars were calculated for each RH value (10, 20, and 30%) using the standard deviations derived from the values obtained in Fig. 3a.

To corroborate the superior vapor sorption behavior, we examined the water sorption isotherm for  $F_3$ @HK\_30 (Fig. 1a). This sample exhibited relatively slower adsorption behavior at a very low relative pressure compared to pristine-HK, probably due to the absence of the chemisorption interaction as determined by in situ Raman spectroscopy (Fig. 2b). Additionally, the pore size distribution (PSD) of the pristine-HK and  $F_3$ @HK\_30 samples were obtained (Supplementary Fig. 18), and the pristine-HK sample exhibited one sharp peak centered at approximately 1 nm, which was similar to those previously obtained<sup>46,47</sup>. In contrast, the PSD of  $F_3$ @HK\_30 exhibited two peaks at approximately 0.7 and 0.85 nm, probably due to the steric hindrance from fluorophenyl oligomers. Therefore, the smaller but still interconnected micropores in the  $F_3$ @HK\_30 sample could be responsible for its high water uptake under low RH conditions (Fig. 1d).

In addition, multi-cycle DVS experiments at 88% RH and 25 °C and desorption by a pressure swing of nitrogen gas at 25 °C were performed for the pristine-HK and  $F_3$ @HK\_30 samples. As expected, the vapor sorption capacity of pristine-HK gradually decreased with prolonged cycling (Fig. 3d). In contrast,  $F_3$ @HK\_30 exhibited a multi-cycle DVS performance, in which the sorption capacity increased slightly at an early stage up to 10 cycles and was well maintained until 76 cycles (more than 300 h) (Fig. 3e). The slight increase in water uptake at the early stage can be attributed to the gradual activation of  $F_3$ @HK\_30 by the initial consecutive pressuring swing process, which captured the ambient moisture prior to the DVS measurement. The multi-cycle performance of  $F_3$ @HK\_30 under high RH conditions was ascribed to its greatly improved hydrolytic stability and fast sorption dynamics.

#### Indoor solar-driven AWH

A solar-driven AWH experiment was conducted in an arid environment using a homemade device based on F<sub>3</sub>@HK 30 infiltrated within

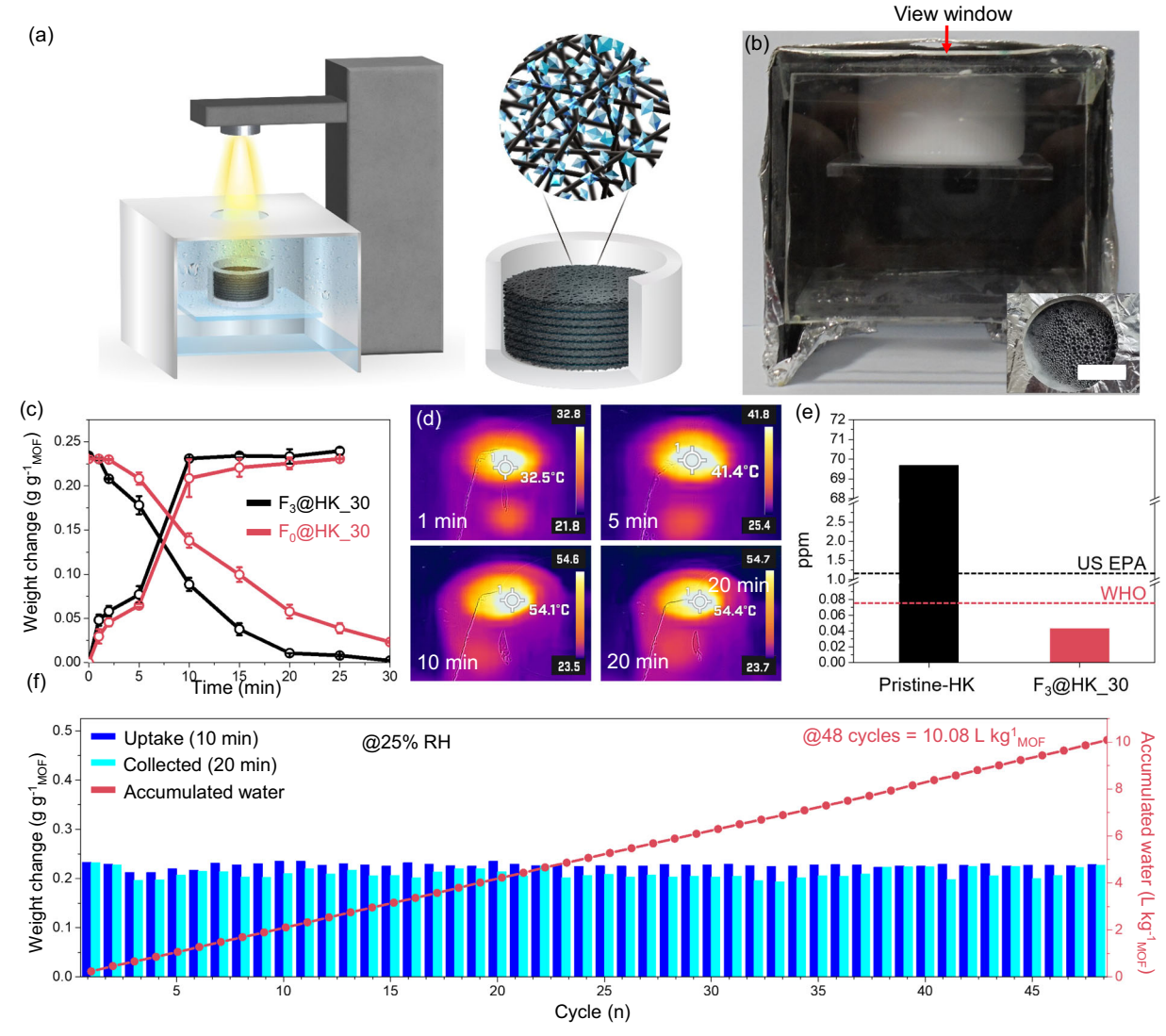


Fig. 4 | Indoor solar-driven AWH of a device based on  $F_3$ @HK\_30 infiltrated within carbon paper ( $F_3$ @HK\_30@CP) at 25% RH and 25 °C. a Schematic illustration of the indoor solar-driven AWH of  $F_3$ @HK\_30@CP located within a styroform@PTFE holder inside a home-made acryl box. b Photograph of a home-made AWH device with the inset showing the top view of the  $F_3$ @HK\_30@CP in the Styroform@PTFE holder. The inset is the photograph of the view window under 1 sun flux after 20 min. The scale bar is 1 cm. c Adsorption and desorption capacities of the AWH device with time. The error bars represent the standard deviation of the

triplicate weight change measurements. **d** Corresponding infrared images indicating the temperature obtained at a particular exposure time (1, 5, 10, and 20 min). **e** Dissolved Cu ion concentrations from the AWH device based on pristine-HK@CP and  $F_3$ @HK\_30@CP in comparison with the US EPA (1.3 ppm) and WHO (2 ppm) standards for drinking water. **f** Multi-cycle (48 cycles) AWH of  $F_3$ @HK\_30@CP with adsorption of dry air (25% RH) at 25 °C and desorption for 20 min under 1 sun flux. Source data are provided as a Source Data file.

carbon paper (F<sub>3</sub>@HK 30@CP, Fig. 4a, b and Supplementary Fig. 19 show an SEM image of the carbon paper) under adsorption conditions of 25% RH and 25 °C and desorption under a 1 sun condition. The CP was 2 cm in diameter, 0.16 mm thick, and 9.2 mg, and the device contained 127.4 mg of F<sub>3</sub>@HK 30. Ten stacks of F<sub>3</sub>@HK 30@CP, located within a styrofoam@PTFE holder inside a homemade acrylic box, were used in the experiment. According to the absorption spectra (Supplementary Fig. 20), F<sub>3</sub>@HK\_30@CP effectively absorbed solar light in the full solar spectral range of 200-2500 nm, whereas F<sub>3</sub>@HK\_30 selectively absorbed light between 550 and 1100 nm. In the adsorption process, the sorption capacity of F<sub>3</sub>@HK 30@CP was 0.23 g g<sup>-1</sup><sub>MOF</sub>, which was completed within 10 min, again confirming its fast sorption dynamics (Fig. 4c). The desorption process was performed under 1 sun condition, where more than 90% desorption was achieved within 20 min (Fig. 4c). Comparably, F<sub>0</sub>@HK 30@CP exhibited similar adsorption kinetics but slower desorption than F<sub>3</sub>@HK 30@CP (Fig. 4c). The experiments were conducted in triplicate, and error bars were calculated for each point using the standard deviation. Considering a similar pore blockage for both samples (Supplementary Table 1), the faster desorption of  $F_3@HK_30@CP$  was attributed to the fluorination effect.

To monitor the increase in temperature of  $F_3@HK\_30@CP$  under 1 sun condition, infrared images were measured over time using an IR camera. As shown in Fig. 4d, the temperature of  $F_3@HK\_30@CP$  increased to approximately 54 °C within 10 min, and then remained constant. In addition, water droplets were clearly observed through the view window after 20 min of desorption under a 1 sun flux (Fig. 4b inset). These results strongly suggest that desorption can be effectively achieved using the low-grade heat generated by sunlight. To elucidate the energy consumption of the desorption process, the heat of adsorption of water vapor for  $F_3@HK\_30$  was measured, and exhibited a moderate value of approximately 55 kJ mol $^{-1}$  (Supplementary Fig. 21), clearly supporting the sun-light-powered desorption process $^{26}$ . One of the major issues of AWH is the leaching of

detrimental components from the adsorbent 18,48,49,, we examined the water desorbed from both pristine-HK@CP and F<sub>3</sub>@HK 30@CP using inductively coupled plasma-mass spectrometry (ICP-MS). The Cu ion concentration of the desorbed water from the pristine-HK@CP was 69.7 ppm; in contrast, only 0.044 ppm of Cu was detected in the water desorbed from the F<sub>3</sub>@HK 30@CP sample (Fig. 4e). The water harvested from F<sub>3</sub>@HK 30@CP was well within the US EPA (1.3 ppm) and WHO (2 ppm) standards for drinking water<sup>50,51</sup>. Thus, it can be concluded that fresh drinking water can be harvested from the F<sub>3</sub>@HK 30-based water harvester through effective protection of the metal center by the hydroxyl oxygen in the fluorophenols and the fluorination effect. Furthermore, multi-cycle solar-driven AWH was performed under adsorption conditions of 25% RH and 25 °C for 10 min and desorption under 1 sun condition for 20 min (Fig. 4f). After 48 cycles (24 h), the adsorption and desorption capacities of F<sub>3</sub>@HK\_30@CP remained intact, and this device was capable of harvesting 10.08 L kg<sup>-1</sup><sub>MOF</sub> without any additional energy input, clearly demonstrating its excellent performance. In addition, the XRD pattern and nitrogen sorption isotherm of the sample were not affected after 48 AWH cycles, confirming the hydrolytic stability of F<sub>3</sub>@HK 30 (Supplementary Fig. 22).

#### **Outdoor solar-driven AWH**

A prototype solar-powered water harvester was proposed to verify the proof-of-concept of the AWH under outdoor condition. It should be noted that the RH during summer in Korea is not as low as that in arid regions. The Styrofoam holder had 5 holes filled with 20 pieces of CP, including F<sub>3</sub>@HK 30 (2.78 g), which was the same size as the sample used in the indoor experiment, and this prototype water harvester was tested on a roof at Hanyang University (Fig. 5a). Notably, because the small-scale AWH device contained only a small amount of F<sub>3</sub>@HK 30 (2.78 g), the desorbed water could not be properly condensed and collected. Thus, the weight difference between the adsorption and desorption of atmospheric water in F<sub>3</sub>@HK 30 was used to determine the water sorption capacity in the multi-cycle outdoor experiments. The adsorption proceeded at ambient RH (approximately 53%) before 7:30 AM and the adsorption capacity of this device was approximately 0.23 g g<sup>-1</sup><sub>MOF</sub>, which was completed within 10 min (Fig. 5b). Desorption was achieved under natural sunlight starting at 7:30 AM, and more than 90% of the adsorbed water was successfully desorbed within 20 min (Fig. 5b). According to the video recorded for the desorption process (Video S1), water droplets on the ceiling were readily observed after 1 min, confirming the fast desorption process for this prototype water harvester. In addition, the temperature of the adsorbent increased to 45.5, 56.5, 57.1, and 58.3 °C after 5, 10, 15, and 20 min, respectively, as measured by an IR camera (Fig. 5c and Supplementary Fig. 23), and the corresponding photograph from the ceiling at 20 min explicitly showed many water droplets on the surface (right top of Fig. 5a). Furthermore, a 22-cycle solar-driven AWH in an outdoor environment was achieved from 7:30 AM to 6:30 PM, with one cycle consisting of 30 min of adsorption-desorption. The temperatures (adsorbent and ambient), RH, and solar flux over the time of day are plotted in Fig. 5d, e.

In attempt to prove the practical applicability of the  $F_3$ @HK\_30 sample, large-scale AWH experiments were conducted in February and May of 2024. A large-scale AWH device consisting of approximately 102 g of  $F_3$ @HK\_30 infiltrated within a polyacrylonitrile-based carbon fabric (CF),  $F_3$ @HK\_30@CF, was placed inside a homemade acrylic box (45 × 40 × 10 cm, Fig. 6a, b and Supplementary Figs. 24 and 25). AWH experiments were conducted on the roof of Hanyang University on May 18 that 15 adsorption (10 min)–desorption (20 min) cycles were achieved. Water drops on the ceiling were clearly observed during the desorption process (Fig. 6c), and 264.8 mL was collected during the daytime using the large-scale AWH device (Fig. 6d), which can be converted to 2.62 L kg $^{-1}_{MOF}$ . The temperature of  $F_3$ @HK\_30@CF under

sunlight was approximately 59 °C (Supplementary Fig. 26), and the profiles of ambient air temperature, RH, and solar flux as functions of time of day are displayed in Fig. 6e. In addition, the water accumulated by the natural sunlight-driven multi-cycle AWH is represented by the time of day (Fig. 6f). The other AWH experiments on May 12 and 19 produced 255.9 and 262.5 mL during the daytime using the large-scale AWH device, which can be converted to 2.51 and 2.59 L kg<sup>-1</sup><sub>MOF</sub>, respectively (Supplementary Figs. 27 and 28). In addition, large-scale AWH experiments were successfully conducted during winter (February 14 and 16), demonstrating the reproducibility of our sample under different environmental conditions (Supplementary Figs. 29 and 30).

Furthermore, we conducted 100 cycles of large-scale AWH experiments in May (May 2, 8, 9, 10, 12, 14, 16, 17, 18, 19, and 22, 2024). Per one cycle of AWH, 13.1–20.7 mL of water were harvested depending on the solar flux of the time of the experiment day (Fig. 6g). Therefore, large-scale solar-driven AHW experiments clearly demonstrated the practical applicability of the  $F_{3}$ @HK 30 sample.

# **Discussion**

VPP was successfully accomplished within pristine-HK, in which open metal sites vulnerable to water vapor were effectively protected by hydroxyl oxygen fluorophenols, while preserving the characteristic water sorption behavior. Among the various FO@HK samples, F<sub>3</sub>@HK 30 exhibited excellent hydrolytic stability at 88 °C and 88% RH for 56 weeks because of the efficient protection of the open metal sites and the fluorination effect. In addition, F<sub>3</sub>@HK\_30 exhibited vapor sorption rates of 3.84, 8.04, and 11.76 L  $kg^{-1}_{MOF} h^{-1}$  at 10, 20, and 30% RH, respectively, which are among the best values to date, clearly confirming its excellent water sorption kinetics. Therefore, this approach can be applied to other conventional moisture-sensitive MOFs with characteristic water sorption behaviors, which can be employed as energy- and time-efficient sorbents for AWH to sustainably provide freshwater in arid areas. In addition, 22 solar-driven AWH cycles were conducted during the day in an outdoor experiment. Finally, the large-scale AWH experiment generated 264.8 mL of water, which was converted to 2.62 L kg<sup>-1</sup><sub>MOF</sub>, clearly demonstrating the practical applicability of the F<sub>3</sub>@HK 30 based AWH device<sup>52</sup>.

#### Methods

# **Materials**

Cu(NO<sub>3</sub>)<sub>2</sub>·2.5H<sub>2</sub>O, Mg(NO<sub>3</sub>)<sub>2</sub>·6H<sub>2</sub>O and paraformaldehyde was purchased from Sigma Aldrich. 1,3,5-Benzenetricarboxylic acid (BTC) and phenol (98%) were purchased from Tokyo Chemical Industry (TCI). N,N-dimethylformamide (DMF) (99%), acetonitrile (99.8%), and sulfuric acid (98%) were purchased from Daejung Chemicals & Metals. Ethanol (99.9%) was purchased from samchun Chemicals. 2,5-dioxidobenzene–1,4-dicarboxylate (DOBDC), 3-fluorophenol, and 2,3,4-tri-fluorophenol were purchased from Alfa Aesar.

#### Synthesis of HKUST-1 (Pristine-HK)

Pristine-HK was prepared as follows. First, the mixture was prepared with  $5\,\mathrm{g}$  of  $\mathrm{Cu(NO_3)_2\cdot2.5H_2O}$  and  $3\,\mathrm{g}$  of BTC in  $150\,\mathrm{mL}$  of DMF. The mixture was completely dissolved in a  $250\,\mathrm{mL}$  polypropylene(PP) bottle until a clear solution was obtained. The solution was then sealed and reacted for  $16\,\mathrm{h}$  in a  $90\,^\circ\mathrm{C}$  convection oven. The resulting product was collected by centrifugation and washed 3 times with DMF and acetonitrile. Finally, pristine-HK was activated at  $100\,^\circ\mathrm{C}$  in a static vacuum to obtain nitrogen and water adsorption isotherms.

#### Synthesis of the FO@HK samples

Pristine-HK was developed into FO@HK using the VPP method. First, pristine-HK, paraformaldehyde, and phenolic precursor were placed separately in a 500 mL glass container with a stopcock. A specific amount (130 mg, Cu: 0.58 mmol) of pristine-HK [Cu<sub>3</sub>(BTC)<sub>2</sub>] was

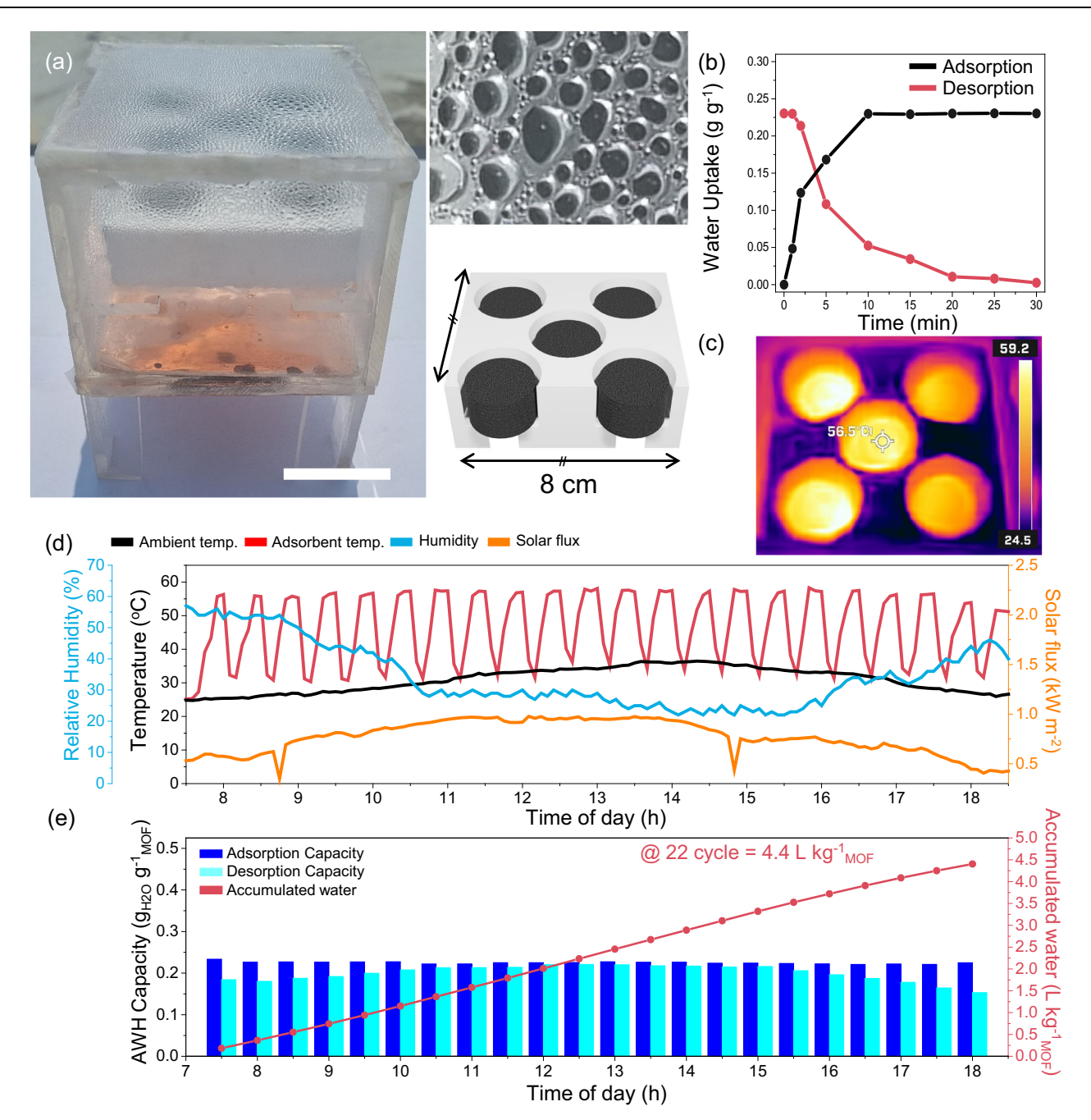


**Fig. 5** | **Outdoor application of the prototype solar-powered water harvester based on F\_3@HK\_30@CP. a** Photograph of a home-made AWH device composed of a styrofoam holder with 5 holes containing 20 pieces of  $F_3$ @HK\_30@CP. The scale bar is 5 cm. Photograph of water droplets on the ceiling after 20 min of desorption by natural sunlight. The bottom right is the schematic image for the styrofoam holder. **b** Adsorption-desorption profiles obtained at ambient RH (approximately 53%) before 7:30 AM (Jun. 3, 2023). The adsorption capacity of this device was approximately 0.23 g  $g^{-1}_{MOF}$ , which was completed within 10 min. The desorption profile of this device was achieved under natural sunlight starting from

7:30 AM. More than 90% of adsorbed water was successfully desorbed within 20 min. **c** The IR camera image for the sample taken outside the device after 10 min of exposure to natural sunlight. **d** Temperature profiles of the adsorbent and ambient air, and RH and solar flux as functions of time of day. **e** 22-cycle natural sunlight-driven AWH starting at 7:30 AM to 6:30 PM with one cycle consisting of 10 min adsorption and 20 min desorption. The collected amounts of water were obtained by measuring the weight differences between adsorption and desorption stages of the water harvester. Source data are provided as a Source Data file.

placed in the reactor with the phenol and paraformaldehyde precursors separately (molar ratio of 1:1.43). Typically, the amount of phenol in  $F_0@HK_100$  was 0.1091g; 1.16 mmol, which allows all Cu open metal sites and phenol to be coordinated and blocks all micropores in pristine-HK. The FO loading levels were adjusted as follows: 0.0054g; 0.058, 0.0164g; 0.174, and 0.0327g; 0.348 mmol of phenol for  $F_0@HK_5$ ,  $F_0@HK_15$ , and  $F_0@HK_30$ , respectively. The  $F_1@HK$  and  $F_3@HK$  samples were prepared similarly. The samples were

polymerized in a 90 °C convection oven for 12 h. The final product was washed three times with acetonitrile and activated in a static vacuum at 70 °C for 6 h to obtain the nitrogen and water sorption isotherms.

#### Synthesis of MOF-74(Mg)

MOF-74(Mg) was prepared as follows. First, the mixture was prepared with  $1.58 \, g$  of Mg(NO<sub>3</sub>)<sub>2</sub>·6H<sub>2</sub>O and  $0.34 \, g$  of DOBDC in a DMF:ethanol:deionized(DI) water =  $150:10:10 \, vol\%$  solution. The mixture was

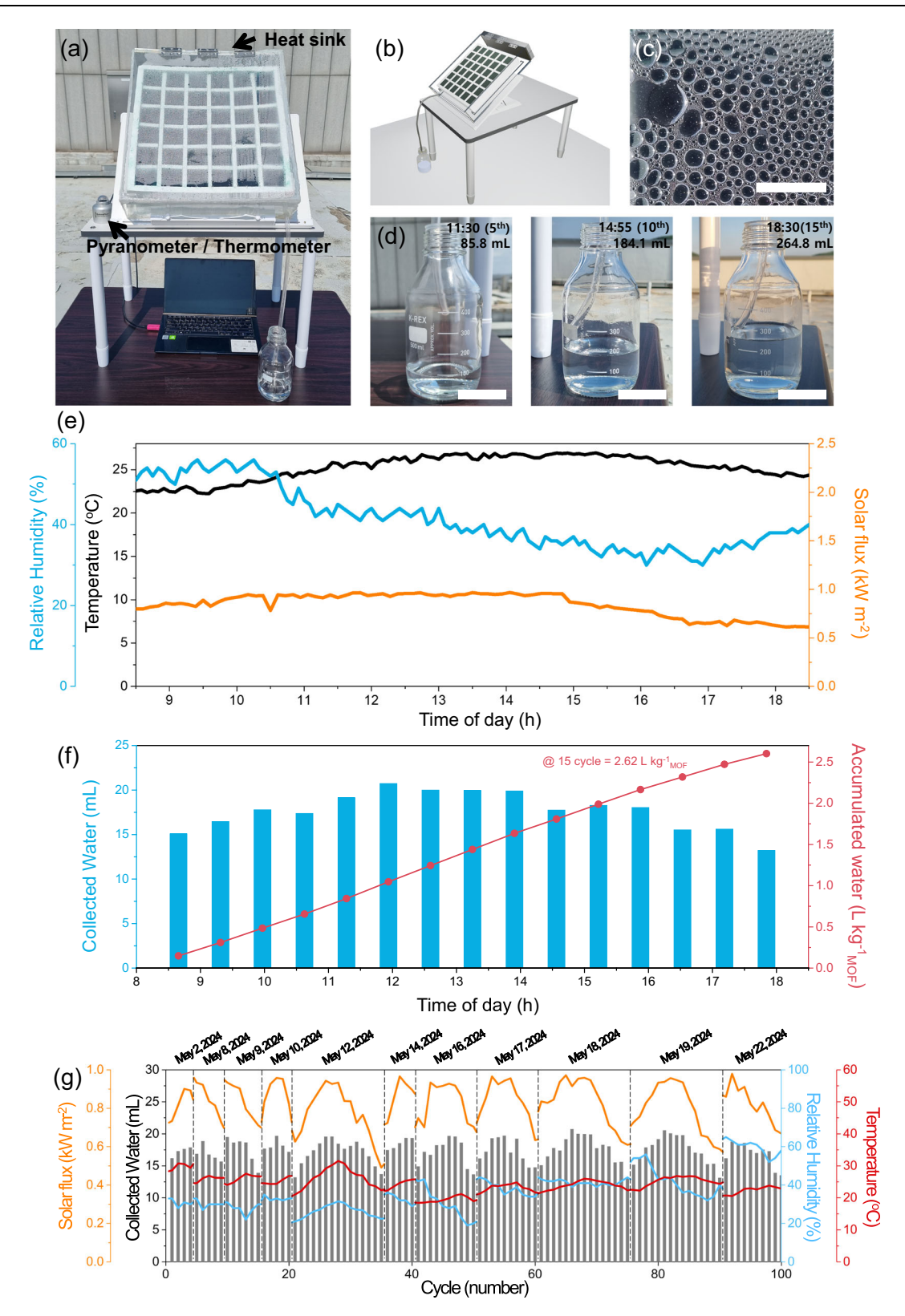


Fig. 6 | Large-scale solar-powered AWH experiment using  $F_3$ @HK\_30@CF at the roof of Hanyang University on May 18, 2024. a Photograph of a home-made large-scale AWH device composed of  $F_3$ @HK\_30@CF located within a styrofoam holder (38 × 38 cm) that had 36 rectangular holes (5 × cm), each of which contained 2 pieces of  $F_3$ @HK\_30@CF. **b** Schematic illustration of the large-scale AWH device. **c** Photograph of water droplets on the ceiling after 20 min of desorption by natural sunlight. The scale bar is 1 cm. **d** Photograph of collected waters with the exact amount from different times of day. **e** Profiles of ambient air temperature, RH, and

solar flux as functions of time of day. **f** Multi-cycle natural sunlight-driven AWH starting at 8:30 AM to 6:30 PM with one cycle consisting of 10 min adsorption and 20 min desorption. The exact amount of water collected during the daytime was 264.8 mL, and 2.62 L kg $^{-1}_{\rm MOF}$  of water harvesting daily using this large-scale AWH device. **g** 100 times of the large-scale AWH experiments during May (2, 8, 9, 10, 12, 14, 16, 17, 18, 19, 22 of May 2024). The harvested amounts of water were 13.1–20.7 mL per one cycle AWH depending on the solar flux of the time of the experiment day. Source data are provided as a Source Data file.

completely dissolved in a 250 mL PP bottle until it became a clear solution. After that, the solution was sealed separately in 6 units of a 40 mL vial and reacted for 24 h in a 120 °C convection oven. The resulting product was collected by centrifugation and washed 3 times with DMF and ethanol. Finally, MOF-74(Mg) was activated at 120 °C in a static vacuum to obtain nitrogen adsorption isotherms.

#### Synthesis of F<sub>3</sub>@MOF-74(Mg) 30

MOF-74(Mg) was converted to  $F_3$ @MOF-74(Mg) via the VPP method. First, MOF-74(Mg), paraformaldehyde, and trifluorophenol were placed separately in a 500 mL glass container with a stopcock. A specific amount (120 mg, Mg: 1.12 mmol) of MOF-74(Mg) [Mg<sub>2</sub>(DOBDC)] was placed in the reactor with the phenol and paraformaldehyde precursors separately (molar ratio of 1:1.43). Typically, the amount of trifluorophenol in  $F_3$ @MOF-74(Mg)\_30 was adjusted to 0.0296 g; 0.2 mmol, which blocks 30% of the micropores in MOF-74(Mg). The sample was then polymerized in a 90 °C convection oven for 12 h. The final product was washed three times with acetonitrile and activated in a static vacuum at 90 °C for 6 hours to obtain nitrogen sorption isotherms.

#### Fabrication of F<sub>3</sub>@HK 30@CP and F<sub>3</sub>@HK 30@CF

 $F_3@HK_30@CP$  and CF were prepared using the following dip-coating method.  $F_3@HK_30$  was dispersed in acetonitrile using a sonicator at a concentration of 0.5 g of  $F_3@HK_30$  per 1 mL acetonitrile. The resulting mixture was then dip-coated on Sigracet 29AA carbon paper (CP, 2 cm in diameter and 0.16 mm thick, and 9.2 mg) or Zoltek FT0500-200 polyacrylonitrile-based carbon fabric (CF, 5  $\times$  5 cm). The dipcoating process was repeated until the loading level was reached at a dry weight of 405.7 g m² for CP and 568.0 g m² for CF. The final weight was determined based on a fully activated state at 90 °C under static vacuum.

#### Sample preparation for the digestion <sup>1</sup>H NMR measurement

A sample of 5 mg of the corresponding  $F_3@HK$  crystals was introduced into an NMR tube containing 1 mL of DMSO- $d_6$  with 0.05 mL  $D_2SO_4$  and thoroughly digested. Preparation was performed in an Ar-charged glove box. The NMR tubes were sealed with plastic caps and acrylic Parafilm prior to removal from the glove box. The integration value of the peaks corresponding to the hydrogen attached to the benzene ring of BTC were used as the internal standard for quantification of phenolic moieties.

#### Measurement of ex situ Raman spectra

Activated HKUST–1 (Act-HK),  $F_3$ @HK\_30 (Act- $F_3$ @HK\_30),  $F_3$ @HK\_15 (Act- $F_3$ @HK\_15), water-coordinated HKUST–1 (H<sub>2</sub>O-HK),  $F_3$ @HK\_30 (H<sub>2</sub>O- $F_3$ @HK\_30), and  $F_3$ @HK\_15 (H<sub>2</sub>O- $F_3$ @HK\_15) were measured. H<sub>2</sub>O-HK samples were prepared by exposing the HKUST–1 crystals to water vapor with the 'vial-in-vial' method, where a smaller vial containing the Act-HK crystals was placed in a capped larger vial containing DI water. We then transferred the samples into disc-shaped quartz cells (Starna, Type 37GS Cylindrical Cells with Quartz to Borofloat graded seal), which were sealed using a glass cork with Apiezon vacuum grease. The entire process described above was conducted under an inert atmosphere in an Ar-charged glovebox.

#### Measurement of in situ Raman spectra

A small amount of the Act-F<sub>3</sub>@HK\_15 and Act-F<sub>3</sub>@HK\_30 samples was transferred to a disc-shaped quartz cell and sealed with a glass cork and Apiezon vacuum grease in a moisture-free argon-filled glove box. After obtaining the initial Raman spectra of Act-F<sub>3</sub>@HK\_15 and Act-F<sub>3</sub>@HK\_30, the quartz cell was opened by removing the glass cork under moist atmosphere. The Raman spectra were then continuously measured while keeping the cell open to expose the Act-F<sub>3</sub>@HK\_15 and Act-F<sub>3</sub>@HK\_30 samples to moist air.

#### Indoor solar-driven AWH

A multi-cycle indoor solar-driven AWH was conducted using an acrylic box containing a disk-shaped  $F_3$ @HK\_30@CP with a diameter of 2 cm, as shown in Fig. 4b. Ten  $F_3$ @HK\_30@CP discs were used, and styrofoam was used to prevent heat loss and ensure an effective temperature increase of the adsorbent. The box with the adsorbent layer was placed in a temperature- and humidity-controlled chamber at 25 °C and 25% RH, with the view window open for adsorption. After 10 min, the amount of water adsorbed was measured using a balance. The cover was then placed on the box, and the system was transferred to a dark room equipped with a 1 sun solar simulator for the 20 min desorption process. The amount of water desorbed was measured using a balance. This process was repeated for 48 cycles to determine the accumulated water desorbed.

#### **Outdoor solar-driven AWH**

The multi-cycle outdoor solar-driven AWH was conducted using an acrylic box containing a styrofoam holder that has 5 holes filled with 20 pieces of CP, including F<sub>3</sub>@HK\_30 (total amount 2.78 g consisting of 2.6 g of F<sub>3</sub>@HK 30 and 0.18 g of CP). This box is the same size as that used in the indoor experiment, as depicted in Fig. 5a. The box, equipped with an adsorbent layer, was placed on the rooftop of Hanyang University. In the shaded area, the box was opened for adsorption, and the amount of adsorbed water was measured using a balance after 10 min. The cover was placed on the box and direct sunlight shone on the system for 20 min to initiate desorption. The amount of desorbed water was determined by measuring the weight change of F<sub>3</sub>@HK 30@CP. This process was repeated 22 times to determine the accumulated desorbed water. A pyranometer (SR05-D2A2, Hukseflux) was used to measure the incident solar flux in the horizontal plane (global horizontal irradiation). The ambient and sample temperatures were measured using a thermometer and an IR camera, respectively, and the RH was measured using a hygrometer.

# Large-scale solar-powered AWH

A large-scale solar-powered AWH was constructed using a custommade acrylic box containing a styrofoam holder. The holder contained 36 rectangular holes filled with pieces of F<sub>3</sub>@HK 30@CF. In total, 72 pieces of F<sub>3</sub>@HK 30@ CF were used (a total amount of 119.5 g consisting of 102.4 g of  $F_3$ @HK\_30 and 17.1 g of CF). The dimensions of the rectangular holes and CF were 5 × 5 cm, and the detailed specifications of the device are shown in Supplementary Fig. 24. The box, along with the adsorbent layer, was placed on a rooftop at Hanyang University, South Korea. The adsorption and desorption processes were conducted by opening the box for adsorption and, after 10 minutes, covering the box and exposing it to direct sunlight for 20 min to initiate desorption. The water desorbed during the process was collected through drains located at the bottom of the equipment, and the water adsorbed on the walls was collected. This process was repeated for 15 cycles to determine the amount of accumulated water. The incident solar flux and ambient temperature were recorded in the same manner as those for the outdoor solar-driven AWH.

# Characterizations

Nitrogen adsorption was measured at 77 K using a Bel Mini adsorption volumetric analyzer (BEL, Japan). All samples were degassed at 80 °C for 6 h under static vacuum. The specific surface area and total pore volume were determined using the Brunauer-Emmett-Teller (BET) method from the nitrogen adsorption isotherms in a relative pressure range of 0.05 0.20. Micropore volumes were calculated using the t-plot method. Water adsorption isotherms were measured at 298 and 343 K using an adsorption volumetric analyzer BEL Max, BEL, Japan). Scanning electron microscopy (SEM) was performed using a HITACHI S-4800 microscope operating at an accelerating voltage of 15.0 kV and an applied current of 10 mA. Powder x-ray diffraction (PXRD) patterns

were recorded using a Rigaku Miniflex600 instrument (Cu Ka,  $\lambda = 1.5406 \text{ Å}$ ). Thermogravimetric analysis (TGA) was performed using an SDT 0600 from TA Instruments Inc. with a heating rate of 10 °C min<sup>-1</sup> under dry air gas flow at 100 mL min<sup>-1</sup>. Fourier-transform infrared spectra were measured on a ZnSe crystal using a Varian FTS 1000 instrument in the attenuated total reflection mode. <sup>1</sup>H-NMR spectra were recorded using an AVANCE III HD FT-NMR spectrometer (Bruker, 400 MHz for 1H). <sup>1</sup>H chemical shifts were referenced to the residual proton resonance of the solvent. The Larmor frequencies for <sup>13</sup>C and <sup>19</sup>F were 100.66 MHz and the spinning rates were 10 and 14 kHz, respectively. The dynamic vapor sorption (DVS) was tested using a DVS Intrinsic manufactured by Surface Measurement Systems. 3 times of measurements were obtained by placing a powdered sample, typically in the range of 14–15 mg, in a sample holder. The DVS Intrinsic was automatically operated to control the relative humidity at 0-88% and temperature at 25 °C. All samples were tested under the condition of adsorption at 10, 20, 30, 88% RH for 3 h and desorption with dry N<sub>2</sub> for 1h. Wavelength dispersive X-ray fluorescence spectrometry was measured using a ZSX Primus II, Rigaku at an accelerating voltage of 60.0 kV and an applied current of 150 mA. Raman spectra were recorded on a Nicolet Almega XR dispersive Raman spectrometer (Thermo Scientific). Indoor solar-driven AWH was conducted using an Abet 1050 solar simulator under standard AM 1.5 illumination at an intensity of 100 mW cm<sup>-2</sup> (Abet Technologies, USA). ICP-MS was performed using an Agilent 7700 instrument equipped with an Ar plasma source. Density functional theory (DFT) calculations were performed using the Vienna ab initio simulation software package (VASP version 5.4.4). Computational details are described in Supplementary Note 1.

# Data availability

The data supporting the findings of the study are included in the main text and supplementary information files. Source data are provided with this paper. All adsorption data, in.aif format, have been deposited in the zenodo repository<sup>53</sup>. Additional data are available from the corresponding author upon request. Source data are provided with this paper.

#### References

- Vörösmarty, C. J., Green, P., Salisbury, J. & Lammers RB. Global Water Resources: Vulnerability from Climate Change and Population Growth. Science 289, 284–288 (2000).
- Mekonnen, M. M. & Hoekstra, A. Y. Four Billion People Facing Severe Water Scarcity. Sci. Adv. 2, e1500323 (2016).
- Kim, H. et al. Water Harvesting from Air with Metal-Organic Frameworks Powered by Natural Sunlight. Science 356, 430–434 (2017).
- Kalmutzki, M. J., Diercks, C. S. & Yaghi, O. M. Metal-Organic Frameworks for Water Harvesting from Air. Adv. Mater. 30, 1704304 (2018).
- 5. Hanikel, N., Prévot, M. S. & Yaghi, O. M. MOF Water Harvesters. *Nat. Nanotechnol.* **15**, 348–355 (2020).
- Xu, J. et al. Ultrahigh Solar-Driven Atmospheric Water Production Enabled by Scalable Rapid-Cycling Water Harvester with Vertically Aligned Nanocomposite Sorbent. *Energy Environ. Sci.* 14, 5979–5994 (2021).
- Fathieh, F., Kalmutzki, M. J., Kapustin, E. A., Waller, P. J., Yang, J. & Yaghi, O. M. Practical Water Production from Desert Air. Sci. Adv. 4, eaat3198 (2018).
- 8. Guo, Y., Guan, W., Lei, C., Lu, H., Shi, W. & Yu, G. Scalable Super Hygroscopic Polymer Films for Sustainable Moisture Harvesting in Arid Environments. *Nat. Commun.* **13**, 2761 (2022).
- Park, K.-C., Chhatre, S. S., Srinivasan, S., Cohen, R. E. & McKinley, G.
  H. Optimal Design of Permeable Fiber Network Structures for Fog Harvesting. *Langmuir* 29, 13269–13277 (2013).
- Klemm, O. et al. Fog as a Fresh-Water Resource: Overview and Perspectives. AMBIO 41, 221–234 (2012).

- Clus, O., Ortega, P., Muselli, M., Milimouk, I. & Beysens, D. Study of Dew Water Collection in Humid Tropical Islands. J. Hydrol. 361, 159–171 (2008).
- 12. Lee, A., Moon, M.-W., Lim, H., Kim, W.-D. & Kim, H.-Y. Water Harvest via Dewing. *Langmuir* **28**, 10183–10191 (2012).
- Gao, S., Wang, Y., Zhang, C., Jiang, M., Wang, S. & Wang, Z. Tailoring Interfaces for Atmospheric Water Harvesting: Fundamentals and Applications. *Matter* 6, 2182–2205 (2023).
- Wang, L. W., Wang, R. Z. & Oliveira, R. G. A Review on Adsorption Working Pairs for Refrigeration. *Renew. Sust. Energ. Rev.* 13, 518–534 (2009).
- Wei, X., Wang, W., Xiao, J., Zhang, L., Chen, H. & Ding, J. Hierarchically Porous Aluminosilicates as the Water Vapor Adsorbents for Dehumidification. *Chem. Eng. J.* 228, 1133–1139 (2013).
- Zhao, F., Zhou, X., Liu, Y., Shi, Y., Dai, Y. & Yu, G. Super Moisture-Absorbent Gels for All-Weather Atmospheric Water Harvesting. Adv. Mater. 31, 1806446 (2019).
- Yao, H., Zhang, P., Huang, Y., Cheng, H., Li, C. & Qu, L. Highly Efficient Clean Water Production from Contaminated Air with a Wide Humidity Range. Adv. Mater. 32, 1905875 (2020).
- Yang, K., Pan, T., Pinnau, I., Shi, Z. & Han, Y. Simultaneous Generation of Atmospheric Water and Electricity using a Hygroscopic Aerogel with Fast Sorption Kinetics. *Nano Energy* 78, 105326 (2020).
- Lu, H. et al. Tailoring the Desorption Behavior of Hygroscopic Gels for Atmospheric Water Harvesting in Arid Climates. Adv. Mater. 34, 2205344 (2022).
- Xu, J. et al. Efficient Solar-Driven Water Harvesting from Arid Air with Metal-Organic Frameworks Modified by Hygroscopic Salt. Angew. Chem. Int. Ed. 59, 5202–5210 (2020).
- Wang, G., Li, Y., Qiu, H., Yan, H. & Zhou, Y. High-Performance and Wide Relative Humidity Passive Evaporative Cooling Utilizing Atmospheric Water. *Droplet* 2, e32 (2023).
- Nguyen, H. L. Covalent Organic Frameworks for Atmospheric Water Harvesting. Adv. Mater. 35, 2300018 (2023).
- Furukawa, H. et al. Water Adsorption in Porous Metal-Organic Frameworks and Related Materials. J. Am. Chem. Soc. 136, 4369–4381 (2014).
- Burtch, N. C., Jasuja, H. & Walton, K. S. Water Stability and Adsorption in Metal–Organic Frameworks. *Chem. Rev.* 114, 10575–10612 (2014).
- 25. Wang, C., Liu, X., Keser Demir, N., Chen, J. P. & Li, K. Applications of Water Stable Metal–Organic Frameworks. *Chem. Soc. Rev.* **45**, 5107–5134 (2016).
- Hanikel, N. et al. Rapid Cycling and Exceptional Yield in a Metal-Organic Framework Water Harvester. ACS Cent. Sci. 5, 1699–1706 (2019).
- 27. Álvarez, J. R. et al. Structure Stability of HKUST-1 Towards Water and Ethanol and their Effect on its CO2 Capture Properties. *Dalton Trans.* **46**, 9192–9200 (2017).
- Carné-Sánchez, A., Stylianou, K. C., Carbonell, C., Naderi, M., Imaz, I. & Maspoch, D. Protecting Metal-Organic Framework Crystals from Hydrolytic Degradation by Spray-Dry Encapsulating Them into Polystyrene Microspheres. Adv. Mater. 27, 869–873 (2015).
- Bak, W., Kim, H. S., Chun, H. & Yoo, W. C. Facile Synthesis of Metal/ Metal Oxide Nanoparticles Inside a Nanoporous Carbon Matrix (M/ MO@C) through the Morphology-Preserved Transformation of Metal-Organic Framework. Chem. Commun. 51, 7238-7241 (2015).
- Kang, M. S. et al. Coarsening-Induced Hierarchically Interconnected Porous Carbon Polyhedrons for Stretchable Ionogel-Based Supercapacitors. *Energy Storage Mater.* 45, 380–388 (2022).
- Kim, H. S., Kang, M. S., Heo, I. & Yoo, W. C. High-Performance Asymmetric Supercapacitors Based on Monodisperse CuO@C Polyhedron Nanocomposites. *Bull. Korean Chem. Soc.* 42, 649–657 (2021).

- Deria, P. et al. Perfluoroalkane Functionalization of NU-1000 via Solvent-Assisted Ligand Incorporation: Synthesis and CO2 Adsorption Studies. J. Am. Chem. Soc. 135, 16801–16804 (2013).
- Nugent, P. et al. Porous Materials with Optimal Adsorption Thermodynamics and Kinetics for CO2 Separation. *Nature* 495, 80–84 (2013).
- 34. Yang, C. et al. Fluorous Metal-Organic Frameworks with Superior Adsorption and Hydrophobic Properties toward Oil Spill Cleanup and Hydrocarbon Storage. *J. Am. Chem. Soc.* **133**, 18094-18097 (2011).
- Al-Muhtaseb, S. A. & Ritter, J. A. Preparation and Properties of Resorcinol–Formaldehyde Organic and Carbon Gels. Adv. Mater. 15, 101–114 (2003).
- Bae, J., Lee, C. Y. & Jeong, N. C. Weak Coordination Bond of Chloromethane: A Unique Way to Activate Metal Node Within an Unstable Metal-Organic Framework DUT-34. *Bull. Korean Chem.* Soc. 42, 658-666 (2021).
- Song, D. et al. Coordinative Reduction of Metal Nodes Enhances the Hydrolytic Stability of a Paddlewheel Metal–Organic Framework. J. Am. Chem. Soc. 141, 7853–7864 (2019).
- 38. Bae, J., Park, S. H., Moon, D. & Jeong, N. C. Crystalline Hydrogen Bonding of Water Molecules Confined in a Metal-Organic Framework. Commun. Chem. 5, 51 (2022).
- Supronowicz, B., Mavrandonakis, A. & Heine, T. Interaction of Small Gases with the Unsaturated Metal Centers of the HKUST-1 Metal Organic Framework. J. Phys. Chem. C. 117, 14570–14578 (2013).
- 40. Xue, W., Zhang, Z., Huang, H., Zhong, C. & Mei, D. Theoretical Insights into the Initial Hydrolytic Breakdown of HKUST-1. *J. Phys. Chem. C.* **124**, 1991–2001 (2020).
- Kim, S., Park, H. & Choi, H. Maneuvering the Ordered Mesoporosity of Electrospun Silica Nanofibers for Water Harvesting. *Microporous Mesoporous Mater.* 281, 23–31 (2019).
- Yang, K. et al. Hollow Spherical SiO2 Micro-Container Encapsulation of LiCl for High-Performance Simultaneous Heat Reallocation and Seawater Desalination. J. Mater. Chem. A 8, 1887–1895 (2020).
- 43. Ni, F. et al. Tillandsia-Inspired Hygroscopic Photothermal Organogels for Efficient Atmospheric Water Harvesting. *Angew. Chem. Int. Ed.* **59**, 19237–19246 (2020).
- Wu, Q., Su, W., Li, Q., Tao, Y. & Li, H. Enabling Continuous and Improved Solar-Driven Atmospheric Water Harvesting with Ti3C2-Incorporated Metal-Organic Framework Monoliths. ACS Appl. Mater. Interfaces 13, 38906–38915 (2021).
- Kim, H. et al. Adsorption-based Atmospheric Water Harvesting Device for Arid Climates. Nat. Commun. 9, 1191 (2018).
- Uemura, T., Kadowaki, Y., Kim, C. R., Fukushima, T., Hiramatsu, D. & Kitagawa, S. Incarceration of Nanosized Silica into Porous Coordination Polymers: Preparation, Characterization, and Adsorption Property. Chem. Mater. 23, 1736–1741 (2011).
- Vishnyakov, A., Ravikovitch, P. I., Neimark, A. V., Bülow, M. & Wang, Q. M. Nanopore Structure and Sorption Properties of Cu–BTC Metal –Organic Framework. *Nano Lett.* 3, 713–718 (2003).
- Yang, J. et al. A Moisture-Hungry Copper Complex Harvesting Air Moisture for Potable Water and Autonomous Urban Agriculture. Adv. Mater. 32, 2002936 (2020).
- Nandakumar, D. K., Zhang, Y., Ravi, S. K., Guo, N., Zhang, C. & Tan, S.
  C. Solar Energy Triggered Clean Water Harvesting from Humid Air Existing Above Sea Surface Enabled by a Hydrogel with Ultrahigh Hygroscopicity. Adv. Mater. 31, 1806730 (2019).
- Khan, K. et al. Health Risks Associated with Heavy Metals in the Drinking Water of Swat, Northern Pakistan. J. Environ. Sci. 25, 2003–2013 (2013).
- Fitzgerald, D. J. Safety Guidelines for Copper in Water. *Am. J. Clin.* Nutr. **67**, 1098S–1102S (1998).
- LaPotin, A. et al. Dual-Stage Atmospheric Water Harvesting Device for Scalable Solar-Driven Water Production. Joule 5, 166–182 (2021).

 Kang, M. S. et al. Time-efficient atmospheric water harvesting using Fluorophenyl oligomer incorporated MOFs. Zenodo. https://doi. org/10.5281/zenodo.13709742.

# **Acknowledgements**

This work was supported by the National Research Foundation of Korea (NRF) grant funded by the Korea government (MSIT) (RS-2024-00347936 (WCY), RS-2024-00409952 (WCY), and NRF-2023R1A2C2004838 (NCJ)), the GRRC program of Gyeonggi Province (GRRCHanyang2020-B01 (WCY)), and the DGIST R&D Program (24-HRHR+-01 (NCJ)). This work was also supported by the Commercialization Promotion Agency for R&D Outcomes (COMPA) grant funded by the Korean Government (MSIT) (RS-2023-00304763 (WCY)). We thank S. Lee for providing the 3D graphic images of the large-scale AWH device.

#### **Author contributions**

M.S.K. synthesized and characterized the FO@HK samples. I.H. conducted the AWH experiments. S.H.P. performed the PXRD and Raman experiments. J.B. conducted water sorption measurement. S.K. supported the synthesis of FO@HK, PXRD, Raman measurements, and AWH experiments. G. K and B.-H. K. performed DFT calculations. M.S.K., I.H., S.H.P., N.C.J., and W.C.Y. wrote the manuscript. N.C.J. and W.C.Y. planned and supervised the project.

# **Competing interests**

The authors declare no competing interests.

#### **Additional information**

**Supplementary information** The online version contains supplementary material available at https://doi.org/10.1038/s41467-024-53853-7.

**Correspondence** and requests for materials should be addressed to Nak Cheon Jeong or Won Cheol Yoo.

**Peer review information** *Nature Communications* thanks Ruzhu Wang, Zuankai Wang, and the other, anonymous, reviewers for their contribution to the peer review of this work. A peer review file is available.

**Reprints and permissions information** is available at http://www.nature.com/reprints

**Publisher's note** Springer Nature remains neutral with regard to jurisdictional claims in published maps and institutional affiliations.

Open Access This article is licensed under a Creative Commons Attribution-NonCommercial-NoDerivatives 4.0 International License, which permits any non-commercial use, sharing, distribution and reproduction in any medium or format, as long as you give appropriate credit to the original author(s) and the source, provide a link to the Creative Commons licence, and indicate if you modified the licensed material. You do not have permission under this licence to share adapted material derived from this article or parts of it. The images or other third party material in this article are included in the article's Creative Commons licence, unless indicated otherwise in a credit line to the material. If material is not included in the article's Creative Commons licence and your intended use is not permitted by statutory regulation or exceeds the permitted use, you will need to obtain permission directly from the copyright holder. To view a copy of this licence, visit http://creativecommons.org/licenses/by-nc-nd/4.0/.

© The Author(s) 2024